DTI-based fibre tracking in the examination of visuomotor networks

Jan Scholz[1]
Supervisors: Pieter Medendorp[1], David Norris[1]

[1]*F.C. Donders Centre for Cognitive Neuroimaging, Nijmegen, The Netherlands*

The ability to follow axonal tracts in white matter using diffusion tensor imaging (DTI) has existed for some years. Only very recently have research groups attempted to combine functional magnetic resonance data (fMRI) with tractographic data obtained with DTI. In this project we assessed the utility of DTI-based fibre-tracking for examining visuomotor networks in healthy human adults. We hypothesized that cortical pathways for oculomotor control can be mapped using a combined DTI-fMRI approach. We used a delayed-saccade task to map the topographic organization of the frontoparietal oculomotor system. Varying the polar angle of the peripheral target for a delayed saccade in a systematic fashion revealed several topographically organized areas in parietal and frontal cortices. Subsequently we attempted to determine anatomical connectivity of these regions, in particular the connections between the human analogues of monkey areas FEF and LIP, with several DTI-based fibre-tracking approaches. Each approach met with limited success.

Keywords: FEF, IPS, oculomotor system, saccades, fibre-tracking

Correspondence to: Jan Scholz, FMRIB Centre, John Radcliffe Hospital, Headington, Oxford OX3 9DU, UK; e-mail: jscholz@fmrib.ox.ac.uk.

1. Introduction

Over the past decades magnetic resonance imaging (MRI) and its specific applications, such as functional blood-oxygenation-level-dependent (BOLD) imaging (Ogawa et al., 1990), diffusion tensor imaging (for a review, see, Le Bihan, 2003) and the tracking of white matter pathways (for a review, see, Mori & Zijl, 2001) have become essential tools in the study of the functional and anatomical organization of the brain. Both methods – fMRI and DTI – have most often been used separately in the past. Functional MRI has been used to study functional networks isolated from the underlying anatomical connections and DTI to investigate white matter tracts without considering the specific functions of the brain areas they connect. Combining fMRI and DTI-based tractography, however, promises to reveal the structural basis of the functional connectivity in vivo. Instead of just adding up the information obtained from both modalities an integrative DTI-fMRI approach uses the functional information to constrain the tractography. Functional data lend themselves to define start and end points of the fibre-tracking process. This method has the advantage that one specifically investigates those fibres that connect regions activated due to a particular task or stimulus. Thus, it seems only natural to combine the independent and complementary information provided by both modalities – the functional activation and the anatomical connectivity – to form a much more comprehensive model of human brain functioning.

In the past, a combined DTI-fMRI approach has most often been applied to a clinical context, such as pre-surgical planning (Parmar et al., 2004; Schonberg 2006) and the investigation of diseases that alter the morphology of white matter tracts (Munakata et al., 2006). A survey of the literature revealed only one combined DTI-fMRI-fibretracking study that included healthy subjects as controls (Guye et al., 2003). The focus on clinical and small case studies is particularly interesting considering the potential wealth of information that such a multimodal approach can provide for neuroscientific research of normal brain functioning. In the present study we assess the utility of a combined DTI-fMRI approach in the context of the healthy adult brain. More precisely, we aim to reveal the functional and structural features of the human oculomotor system. The oculomotor system especially lends itself for this approach, because it is well defined and has been shown to be similar between macaque and human species (Koyama et al., 2004). This correspondence will allow us to draw conclusions about the human oculomotor system on basis of macaque data acquired with methods unavailable for the human (e.g. anatomical tracers).

The primate oculomotor system involves, aside from subcortical components such as basal ganglia, thalamamus, midbrain and cerebellum, a limited number of well defined cortical areas that are distributed over frontal and parietal cortices (Munoz, 2002). In the macaque the most important frontal components consist of the frontal eye fields (FEF) in the lateral prefrontal cortex and the supplementary eye fields (SEF) in the medial prefrontal cortex. The parietal cortex contains another major oculomotor area in the lateral bank of the intraparietal sulcus (IPS), the so-called lateral intraparietal area (LIP). In post mortem tracer studies, all of these areas have been shown to be anatomically connected in the monkey (Lewis & van Essen, 2000; Schall et al., 2004; Stanton et al., 1995). The putative human homologues of these areas have been suggested in the fMRI literature (Astafiev et al, 2003; Koyama et al., 2004, Sereno et al., 2001). The network of cortical oculomotor areas has been demonstrated to be similar between humans and non-human primates using fMRI (Astafiev et al., 2003; Koyama et al., 2004). The parietal cortex might constitute an exception to this rule. Schluppeck et al. suggested that several saccade-related areas can be found along the human IPS (Fig. 1), whereas only one oculomotor area has been found in the monkey.

Recently, various reports demonstrated that at least two of the cortical oculomotor regions are topographically organized in the human (Hagler & Sereno, 2006; Schluppeck et al., 2005; Sereno et al., 2001). Hagler & Sereno et al. (2006) showed that remembered saccade target location in contralateral visual space is systematically arrayed over a well defined region in the lateral prefrontal cortex. Sereno et al. found at least one region with similar topographic properties in the IPS. The connectivity of the human oculomotor system has not been determined so far.

In the present study we employ two experimental paradigms to reveal the cortical components of the human oculomotor system. A standard block design experiment in which blocks of saccades are contrasted with blocks of fixation will allow us to define the human homologues if monkey

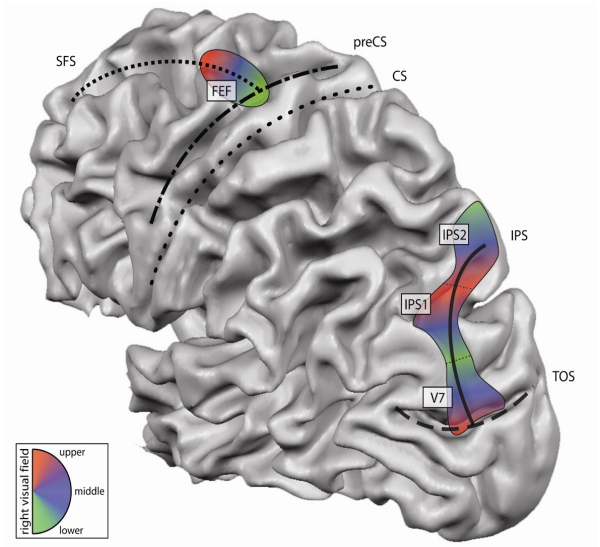

Figure 1. Topographic areas of the human oculomotor system in frontal and parietal lobes. The human oculomotor system comprises at least two major areas that include maps of remembered saccade target locations of the contralateral visual field: the frontal eye field (FEF) and areas along the IPS, such as IPS1 and IPS2. The colour map represents the phase angle of the remembered saccade targets (red, upper right visual field; blue, right horizontal; green, lower right). Retinotopic visual areas are usually coactivated during saccade tasks. Except for V7 they are not shown here for clarity. (CS = central sulcus; IPS = intraparietal sulcus; preCS = precentral sulcus; SFS = superior frontal sulcus; TOS = transoccipital sulcus)

FEF and SEF with high statistical power. A second phase-encoded paradigm will allow us to map the topographic organization of the fronto-parietal regions. In a phase-encoded paradigm spatially-specific stimuli are presented in a systematic and periodic fashion in order to successively activate the entire visual field representation. If multiple joined regions exist along the IPS, the phase-encoded paradigm will have the additional benefit of distinguishing different areas according to the orientation of the visual field representation (Fig. 1). Successfully identified oculomotor regions are then used as seed and target regions for fibre-tracking of the cortical pathways of the visuomotor system

We hypothesize that, similar to the monkey, connections between oculomotor regions in the frontal cortex and oculomotor regions in the parietal cortex exist in humans (e.g. between FEF and IPS), which can be revealed with a combined fMRI-DTI approach. To achieve this objective we will first map the human saccade-related areas using a delayed saccade task in a block design and a phase-encoded experiment. Second, we will use the functional data to constrain the fibre-tracking, in order to reveal the connectivity of the human oculomotor system. Several different fibre-tracking procedures, such as standard streamline tracking and probabilistic tracking will be used and evaluated. Third, we will investigate whether the fibres connect regions which represent the same part of the visual field. This will give us a more fine grained view at the connectivity and reveal whether the topography of visuomotor regions is sustained by the topography of the connecting fibre tracts while simultaneously being a benchmark for the accuracy of the combined fMRI-DTI approach.

The remainder of this introduction will explain the background of the methods employed. This includes an in-depth explanation of diffusion image acquisition, diffusion models, and fibre-tracking. We will close the introduction with a comment on the limitations associated with DTI-based fibre-tracking.

2. Diffusion tensor magnetic resonance imaging (DT-MRI)

2.1 Introduction to DT-MRI

Diffusion tensor magnetic resonance imaging, abbreviated as DT-MRI or just DTI, allows us to study white matter connections between different parts of the brain noninvasively (for a review, see, Bammer et al., 2003). More precisely, DTI refers to the production of MRI-based quantitative maps of microscopic, natural displacements of water molecules that occur in brain tissues as part of the physical diffusion process. The natural displacement of water molecules is systematically affected by tissue structures. The resulting anisotropic diffusion is hypothesized to reflect the organization and orientation of white matter fibre bundles (Beaulieu, 2002). This local information can be used to globally reconstruct axonal tracts (Mori & Zijl, 2002).

The following sections will briefly describe the diffusion imaging process and the relationship of the diffusion weighted images (DWI) to the underlying white matter structure and how this data can be modelled to further the fibre-tracking process. We will end this chapter with a discussion of the problems associated with data acquisition, model, and tracking.

2.2 Data acquisition and diffusion models

Diffusion weighted imaging is based on the fact that molecules perform random translational movements due to the thermal energy they carry. The random displacement of molecules in a free medium (Brownian motion) can be described by a three-dimensional Gaussian distribution and depends on the molecules' mass, the temperature and the medium's viscosity.

Formally, an unrestricted diffusion process is described by the so-called diffusion coefficient, *D*, which is related to the root mean square displacement (RMSD) of freely diffusing molecules over time t_{dif} by $RMSD = (6\ D\ t_{dif})^{1/2}$. The diffusion coefficient measured by nuclear magnetic resonance is known as the apparent diffusion coefficient (ADC). It is not only dependent on the actual diffusion coefficient of the water molecule population present in the voxel, but also on flow and transfer phenomena as well as on experimental parameters, such as the voxel size.

During typical diffusion times of about 50 to 100 ms, water molecules have a high probability of interacting with tissue components, such as the cell membranes or the cytoskeleton. If molecular displacements are no longer uniform in space (i.e. isotropic), diffusion is called anisotropic (i.e. directionally dependent). Consequently, diffusion is no longer sufficiently characterized by a scalar ADC. Instead a symmetric second-order tensor, called the apparent diffusion tensor **D**, is used to approximate the distance and the direction of the diffusing water molecule population. The diffusion tensor can be represented by an ellipsoid (Fig. 2, I). Main, medium, and minor axes of the ellipsoid correspond to the tensor's eigenvectors e_1, e_2, e_3 and the respective eigenvalues λ_1, λ_2, λ_3. The eigensystem is conventionally ordered according to the size of the eigenvalues ($\lambda_1 \leq \lambda_2 \leq \lambda_3$).

Evidence suggests that the tightly packed parallel arrangement of multiple axon membranes and to a lesser degree their myelin sheaths cause the observed anisotropy in white matter by hindering water diffusion perpendicular to the long axis of the fibres relative to the preferential parallel direction (Beaulieu, 2002). If this assumption holds true, it would in principle be possible to infer local fibre direction by measuring water diffusion along different directions. Because magnetic

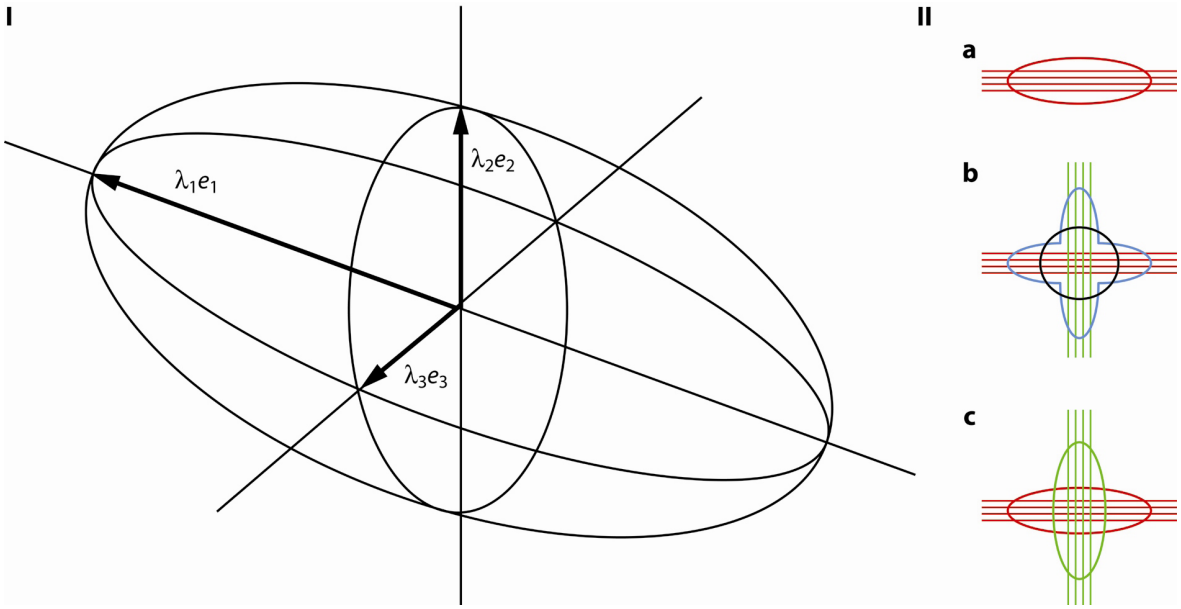

Figure 2. (I) Three-dimensional probability function of anisotropic diffusion depicted as an ellipsoid. The arrows point along the eigenvectors (e1, e2, e3) and are scaled proportionally by their corresponding eigenvalues (λ1, λ2, λ3). The eigensystem is conventionally ordered so that λ1 > λ2 > λ3 holds true. Anisotropic diffusion is characterized by λ1 > λ2 > λ3 and isotropic diffusion by λ1 ~ λ2 ~ λ3. (II) Single and two-tensor models in the case of one or two crossing fibre populations. (IIa) illustrates that a single-tensor is a good local approximation of uniformly oriented fibres (i.e. the overall diffusion process occurring in intra- and extracellular compartments at this location). (IIb) shows that the single-tensor model fails if multiple fibre directions are present within one voxel. The model represents neither of the fibre populations correctly (black circle). The actual diffusion process more closely resembles the blue shape. In (IIc) two well-distinguishable fibre populations are quite accurately modelled by two tensors.

resonance measurements of diffusion are sensitive to molecular displacements along the axis of the diffusion-sensitizing gradients, diffusion along different directions can be evaluated by varying the orientation of the diffusion-sensitizing gradients. At least six different directions are required to characterize the diffusion tensor. Measuring a large number of directions (30-90) reduces signal-to-noise dependence on directions and increases the angular resolution needed to separate crossing fibres.

2.3 DTI-based fibre-tracking

The aim of the fibre-tracking process is to link the local tensor information in such a way that the resulting "virtual" fibres match the underlying neuroanatomy and/or connection probability between different regions can be inferred. There are in principle two different classes of tracking algorithms: deterministic tracking and probabilistic tracking. Both work with but are not exclusive to the tensor model. Deterministic tracking is a subset of probabilistic tracking. It is deterministic in the sense that repeated tracking, starting from the same location, will always follow the same path (Fig. 3, Ia,b). In contrast, probabilistic tracking tracks also less likely directions, determining from each voxel' s diffusion profile the likelihood of a certain fibre direction in that voxel (Fig. 3, Ic). In the following, both types of fibre-tracking approaches and their limitations are described in more detail.

One of the most common classes of deterministic tracking methods is the so-called line-propagation technique, such as the streamline algorithm known from flow computations (see, e.g., Basser et al., 2000; Mori & Zijl, 2002). It consists of three parts: seed point selection, fibre propagation and termination. Seed points are specified by a region of interest (ROI) which can be generated on the basis of anatomical or functional data. Usually more than one streamline is seeded per voxel. The fibre is then propagated through the tensor field assuming that the normalized first eigenvector (e_1),

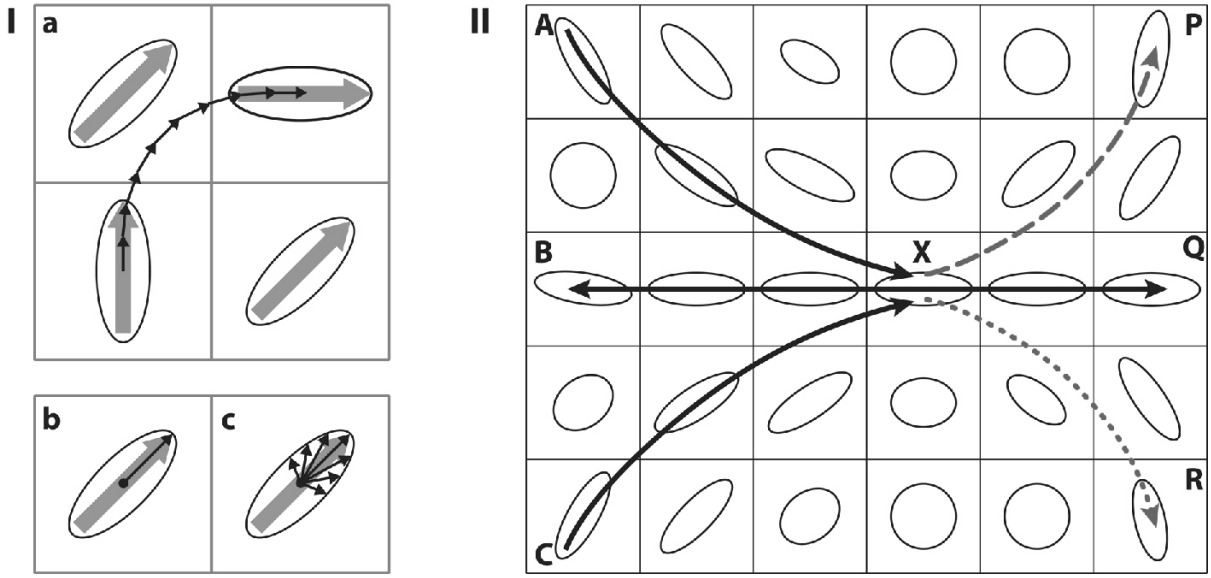

Figure 3. Schematic diagram of the fibre-tracking process and its limitations drawn in two dimensions. In (Ia) fibre-tracking is initiated in the lower left voxel. Ellipses represent a set of sampled diffusion tensors. Large arrows represent the orientation of the major eigenvectors. A fibre is propagated in a stepwise fashion through the interpolated tensor field (small black arrows). Often step sizes smaller than the voxel size are used to achieve higher accuracy. Below, the difference between deterministic (Ib) and probabilistic tracking (Ic) is illustrated. For multiple transitions of the same voxel identical directional information is used during deterministic tracking. For probabilistic tracking the directional information can vary between multiple transitions of the same voxel. (II) shows principle limitations of deterministic fibre tracking algorithms. First, the tracking is non-commutative (Dougherty et al., 2005). Fibres starting in A, B, and C will all converge onto a common point Q. But seeding Q will result in one fibre connecting only Q with B. Second, tracking is problematic in regions of crossing and kissing fibres. As soon as fibres seeded in A,B, and C have reached point X they will be propagated further up to point Q. The underlying neuroanatomy might, however, be different. The fibre starting in A might just kiss fibre BQ in X and continue to P or it might cross BQ at X and continue to R.

which is associated with the largest eigenvalue (λ_1) of the diffusion tensor, lies in parallel to the local fibre tract direction (Bammer et al., 2003).

Higher-order integration schemes, such as the fourth-order Runge-Kutta method, are used to determine the direction of the streamline propagation. These integration schemes require repeated tensor interpolation to derive a tensor at an arbitrary position. This allows for sub-voxel step sizes which increase the overall accuracy of the tracking (Fig. 3, Ia). The propagation continues until a stopping criterion is reached. This can either be a threshold based on fractional anisotropy (FA) or curvature. The former case represents the situation where no clear directionality is defined anymore and the latter the situation where the fibre follows a sharp bend that is assumed to be anatomically implausible.

Most probabilistic tracking approaches are very similar to deterministic line-propagation approaches. They include seed points, line-propagation, and stopping criteria, but differ in three important ways. First, multiple, often thousands of lines are propagated from each point and, second, the directional information used for the line-propagation is varied non-deterministically from pass to pass. Third, the output consists of a map that represents the probability of connection between seed and target points (Fig. 8, G, H). A deterministic line-propagation algorithm will only reveal whether there is a connection or not[1].

Probabilistic tracking is achieved by utilising the Monte Carlo method. Starting from the same point fibres are propagated multiple times through the tensor field while varying the estimated fibre orientation in the traversed voxels in a stochastic way. The estimated fibre orientation is not completely random but determined by the voxel' s probability density function (PDF). The PDF describes the local uncertainty in fibre orientation. There are several ways to define these PDFs. The most straightforward is to interpret the tensor shape as a probability distribution (Koch et al., 2002) (Fig. 3, Ic). The process is equivalent to letting a particle diffuse through the tensor field with the probability of a jump in a particular direction from a given voxel being based on the voxel's PDF. This approach has the advantage that if the local tensor is indeterminate (i.e. disc- or sphere-like) several possibilities will be explored, instead of just heading into a "random" direction. In other words, while deterministic tracking tries to eliminate the inherent noise in the data and find the one "true" fibre direction, probabilistic tracking takes into account the inherent ambiguity of the underlying diffusion imaging data, in the sense that it tries to interpret the data in terms of the likely underlying fibre structure.

In summary, probabilistic tracking can be seen as a superset of deterministic tracking. It combines the basic ingredients of deterministic line-propagation algorithms with the Monte Carlo method. While deterministic streamline tracking yields "virtual" fibres similar in appearance to real fibre tracts, probabilistic tracking makes explicit use of the ambiguous diffusion data to track also in less probable directions. However, the probability maps, produced by the probabilistic approach, are often diffuse and require further interpretation.

2.4 Limitations of DTI-based fibre-tracking

There are basically three possibilities for fibre tracking to fail: data, model, and the tracking itself. The data might prevent the tracking of certain fibre pathways because its resolution is too low or due to noise and distortions. Standard diffusion protocols have a resolution of 1.5 to 3.0 mm^3. This is far removed from the dimensions of myelinated axons in the central nervous system, which have a diameter of roughly 2.5 μm (Alexander, 2006), so that any cubic millimetre of white matter is traversed by about 10^5 axonal fibres. Aside from the averaging of fibres with different orientations within a voxel, one can expect partial volume effects between different tissue types (e.g. grey/ white matter, cerebrospinal fluid). Ultimately, this means that the sampled diffusion profile will no longer accurately represent the underlying fibre structure. Distortions can also hinder fibre tracking. Especially in deeper brain areas and near aerial cavities, magnetic susceptibility artefacts produce large distortions. Eddy current distortions can be partially corrected for (Jezzard and Balaban, 1995). Noise in the data affects the reliability with which multiple fibre directions within a voxel may be resolved, especially at small angular separations. Regularization or averaging of multiple sets of diffusion weighted data can help to reduce the noise in the data.

The modelling process takes centre stage in DTI-based fibre-tracking. On the one hand the

1 It is possible to define a quasi-probability of connection for a deterministic fibre-tracking approach by calculating the ratio between all fibres leaving a certain area and the number of those hitting the target area.

model is limited by the quality of the data, on the other hand the model limits the fibre-tracking process. The single-tensor model assumes that water diffusion is Gaussian. While this holds in cases where all fibres in a voxel are oriented in parallel, it is a poor approximation where fibres cross, diverge, or have high curvature. Therefore, the single-tensor model can resolve only a single fibre orientation within each voxel. Tracking through regions of crossing fibres can be improved by fitting different models, such as the q-ball model (Tuch, 2004) or increasing the number of tensors fitted per voxel (Fig. 2, IIc). It should however first be determined if the quality of the data allows advanced diffusion models. If the angular resolution is too low (i.e. the number of imaged directions is small), fitting more than one tensor will hardly improve the tracking. On the contrary, tracking results might even deteriorate, because the multi-tensor models are more susceptible to noise. In practice, q-ball and multi-tensor models can represent more than one fibre population per voxel, but the quality of the data often limits them to represent no more than two fibre populations per voxel.

The tracking itself can encounter multiple problems, because it basically tries to follow a continuous tract through noisy, discrete DT-MRI data. Interpolation and propagation are prone to errors at discontinuities and singularities in the tensor field. The well known "crossing and kissing fibres"-problem can lead to erroneous tracts (false-positive) or might miss tracts (false-negative). Fibre tracking is especially challenging near the cortical surface where the previously large and consistently organized white matter tracts tend to be more dispersed and anisotropy values lower (Mori & Zijl, 2002).

A general problem of today's fibre tracing methods is their validation. Well-defined probabilistic tracts usually indicate low uncertainty in fibre orientation, while diffuse or dispersing tracts reveal noise or problems with the diffusion model. But this is a highly subjective assessment. It has been suggested to cross-reference the results with known anatomy or animal models. However, these might be incomplete or false. To date, it is therefore not possible to classify tracts as likely true positive or false positive *per se*. Particularly, finding no connection does not necessarily indicate that the tract is absent in the anatomy.

In summary, DTI-based tractography is limited compared to tracer injection techniques that can be used in nonhuman animals or post mortem in humans (Bürgel et al., 2006). It can reveal the global course of white matter fibres only indirectly and it cannot determine the cortical layer in which they terminate. Fibre tracking is especially difficult through regions where the distribution of fibre direction is nonuniform (i.e. where fibres branch, cross or kiss). Probabilistic fibre tracking can often provide a quantitative estimate of connection probability between some of the regions which show no connection in standard streamline tracking. However, interpretation of probabilistic tracking is often difficult, especially when the resulting probability maps are diffuse and widespread. Scanning at higher spatial resolution, imaging more directions, and using advanced imaging and modelling techniques can help to avoid some of the problems, but might still fail in regions with crossing and branching fibres and near the cortical surface. Despite these difficulties DTI-based tractography has enabled us to reveal major white matter tracts of the human brain in vivo (Wakana et al., 2003) and classifying brain structures according to their connectivity (Behrens et al., 2003a; Croxson et al., 2005).

3. Methods

3.1 Subjects

Six healthy subjects (two female; four male; age range, 22-36) participated in the experiments. All had normal or corrected-to-normal vision and gave written informed consent. All subjects completed one scanning session.

3.2 Stimuli and Task

Stimuli were presented using an LCD projector (EIKI LC-X986; 60 Hz; resolution, 1024×768) onto a back-projection screen at the rear-end of the scanner. Subjects viewed the screen indirectly via a 45°-tilted half-silvered mirror above the eyes. Presentation software (Neurobehavioral Systems, Albany, CA, USA) was used for stimulus presentation. An eyetracker (MEyeTrack, SMI, Berlin, Germany) which was situated at the foot end of the patient table recorded eye movements via a second 45°-tilted mirror, which was mounted above the first. Eye movements were recorded to confirm behaviour. Subjects were supine and could comfortably see the whole range of projected stimuli (maximum eccentricity, 11.5°).

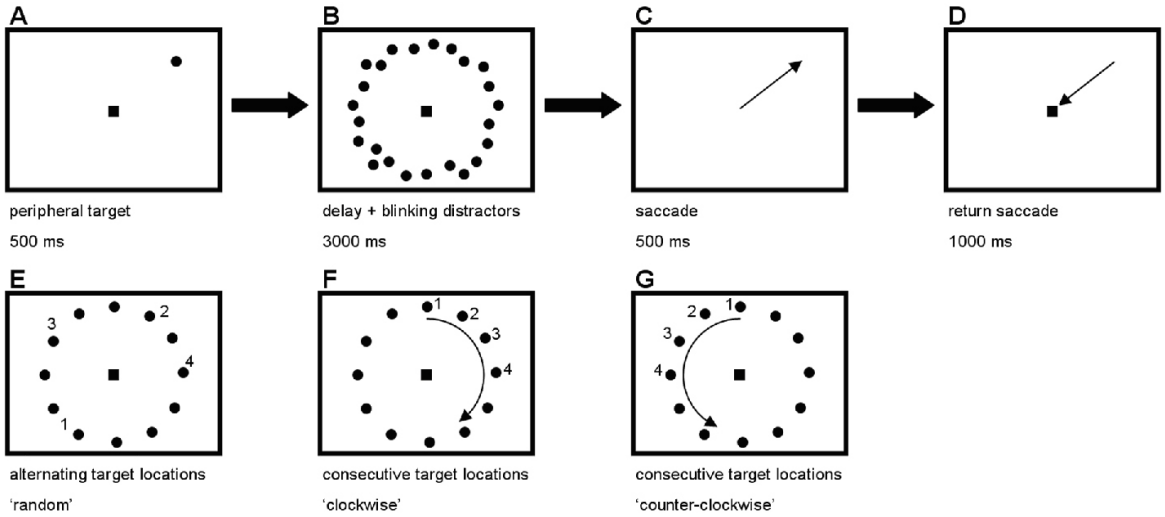

Figure 4. Visual stimuli. The first row (A-D) illustrates the visual stimuli shown to the subject during one trial of 5 s. The second row shows how target position varies between successive trials. During the random saccade task targets appear randomly at one out of 12 possible positions on the target circle (E). During the phase-encoded task targets occur at consecutive positions. More precisely, if during the first trial the target was presented at position one, then the target would be presented at position two in the second trial and so on (F, G). Target always advance in clockwise (or counter-clockwise) direction for five whole circles before the direction is changed to counter-clockwise (or clockwise).

Subjects had to perform a delayed saccade task which was incorporated in two different test paradigms. In each paradigm a target appeared on a circle with 10° eccentricity (eccentricity jitter, ± 1.5°) at one out of 12 possible locations which were separated by 30°, similar to the position of full hours on a clock-face (Fig. 4, E). Target angle was jittered by ±5° to make the target location less predictable. Each trial started with the presentation of the peripheral target for 500 ms, while subjects fixated a central point (A). Then a ring of 200 random, target-sized distractors (eccentricity jitter, ±1.5°) flashed (at 5 Hz) for 3000 ms, while the subject maintained fixation (B). After the disappearance of the distractors and the fixation spot, subjects made a quick saccade to the remembered target location on a black screen (C), followed by an immediate return saccade to the reappearing fixation spot, which subjects continued fixating in preparation of the next trial for 1000 ms (D). Each trial lasted 5 s.

The delayed-saccade task was incorporated in two test paradigms. During the first paradigm, the random saccade paradigm, target position was varied randomly (G) from trial to trial. Blocks in which six saccades had to be executed alternated with blocks of central fixation. The length of both blocks was 30 s. Altogether there were 20 blocks. After 10 blocks there was a break of 45 s during which subjects could freely move their eyes and blink. This paradigm lasted 10 min and 45 s.

In the second paradigm, the phase-encoded paradigm, target position was varied consecutively between trials. In the clockwise condition, the target would appear at 12 o'clock during the first trial and then at 1 and 2 o'clock during the second and third and so on (F). In the counter-clockwise condition, target positions were 12, 11, and 10 o'clock during the first three trials (G). Five cycles of clockwise target progression alternated with five cycles of counter-clockwise target progression. Each cycle required 12 saccades. Blocks of five cycles were separated by breaks of 45 s. The whole second paradigm lasted 45 min and 25 s.

3.3 MRI scanning procedure

All experiments were performed using a 3T Trio whole body scanner (Siemens, Erlangen, Germany). An eight-channel headcoil was used for signal reception. Subjects were stabilized with foam padding.

For each subject we acquired 36 axial slices using a standard gradient-echo EPI sequence (repetition time (TR), 2500 ms; echo time (TE), 35 ms; inversion time (TI), 1100ms; matrix size, 64 × 64; field of view (FoV), 192 mm; isotropic voxels, 3.0 mm; distance factor, 10%)

For each subject we acquired an additional 65 diffusion weighted images using a twice-refocused

spin echo diffusion sequence (Reese et al., 2003) (50 axial slices; TR = 6100 ms ms; TE = 87 ms; matrix size = 64 × 64; FoV = 192 mm; isotropic voxels, 3.0 mm, scan time: 6:43 min). These included five images with no diffusion weighting (*b*-value = 0 s mm-2) and 60 diffusion-weighted images (*b*-value = 1000 s mm-2) along 60 non-collinear directions (Jones et al. 1999). The signal-to-noise ratio in the diffusion weighted images was approximately 20. Resolution and position of the diffusion weighted images was chosen to match the functional protocol in order to minimize differences in distortions between the two protocols.

Finally, a high resolution structural image was collected using a standard T1 MPRAGE sequence (176 saggital slices, TR = 2300 ms, TE = 3.93 ms, matrix size = 256 × 256, FoV = 256 mm, voxel size = 1.0 mm^3, scan time: 9:50 min). This image served as an anatomical reference for the functional data.

3.4 Data analysis

3.4.1 Pre-processing of functional and diffusion data

Functional MRI data were processed using BrainVoyager QX 1.4 software (BrainVoyager QX, Brain Innovation, Maastricht, Netherlands). Data from the first 10 s of each fMRI scan were discarded. Pre-processing of the remaining data included 3D motion correction, slice scan time correction, linear trend removal, and high-pass filtering.

DTI data were processed using SPM (Wellcome Department of Cognitive Neurology, Institute of Neurology, London, UK) and the Stanford VISTA software (http://white.stanford.edu/software/) executed in Matlab (Mathworks, Natick, MA). Basic pre-processing included coregistering all images to the first b_0-weighted image and skull stripping with BET (part of the FSL package; Smith, 2002). Advanced processing included the calculation of tensors maps and fractional anisotropy maps. Finally, deterministic streamline fibre-tracking was performed with VISTA. For comparative purposes, probabilistic tracking was done using the method proposed by Koch et al. (2002). In addition, we performed the advanced processing part with the Camino software package (Cook et al., 2006), to visualize tensor maps and perform two-tensor deterministic streamline tracking.

Anatomical images were transformed into Talairach space, segmented at the gray-white matter boundary and inflated for visualization purposes. Finally, pre-processed functional and diffusion data were coregistered to the high resolution anatomical image to establish a common coordinate space.

3.4.2 Statistics: fMRI

Statistical analysis of the functional data was performed using BrainVoyager QX 1.4 software. The data of the random saccade paradigm were analysed with a single study general linear model (GLM) for each subject separately. Two regressors were defined, one for saccade blocks and one for fixation blocks. The box-car-shaped regressors were convolved with a two-gamma haemodynamic response function (HRF) with a time to response peak of 5 s (time to undershoot peak, 15 s; response undershoot ratio, 6). We contrasted the saccade condition with the fixation condition and plotted the t-values on the inflated brain surface.

The data of the phase-encoded paradigm were analysed per subject using a box-car function convolved with a one-gamma HRF (delta, 2.5; tau, 1.25; n, 3) (Boynton et al., 1996). The HRF was shifted by TR (2.5 s) so that 12 shifts would cover exactly one visual hemifield (30 s). Significantly activated voxels for each lag were colour-coded for lag time (i.e. visual angle of target location). The resulting linear correlation maps for clockwise and counter-clockwise stimuli were subsequently averaged by inverting the lag time association of one map and averaging them over correlation values. The minimal cross correlation threshold was adjusted between 0.1 and 0.08 for each individual subject in order to remove as much noise as possible without degrading the maps.

We used prior knowledge about the anatomical location and topographic organization of higher visual areas (Orban et al., 2004) and visuomotor areas (Schluppeck et al., 2005) to define areas V3A, V7, IPS1, and IPS2 on the inflated cortical surface. An additional tentative area IPS3 was defined if another phase reversal (i.e. reversal of the visual field representation) occurred on the anterior border of IPS2. Further more, we also defined areas that included the adjacent upper (or lower) visual field representation of neighbouring areas (i.e. V3A/V7 upper, V7/IPS1 lower, IPS1/IPS2 upper).

3.4.3 Statistics: Fibre tracking

The regions of interest (ROIs) that were defined on the basis of the functional data (see above) were

used as seed regions for streamline and probabilistic fibre tracking. Seed regions extended orthogonal to the cortical surface three millimetres into white matter and one millimetre into grey matter.

For streamline fibre-tracking we used a maximum threshold angle of 50° that would minimize spurious connections. A conservative FA threshold of 0.15 was chosen to minimize improbable fibres connections across sulcal gaps, while at the same time allowing for enough streamline propagations to start. For each voxel four streamlines at four different positions equidistant from the voxel centre were seeded (step size, 0.5 mm; fourth-order Runge-Kutta interpolation).

Due to the highly convoluted cortical surface, it is, in general, difficult to define which fibres "hit" another ROI. We counted a hit each time a fibre terminated in a target area (i.e. in any other ROI). We excluded fibres that were only passing through a target area, since this situation might arise when a target area picks up deeper long-range association fibres.

We looked at the connections between topographic areas V3A, V7, IPS1, IPS2, IPS3, and FEF within and between hemispheres. We did the same for the upper and lower visual hemifield representations FEF lower, FEF upper, V3d/V3A lower, V3AV7 upper, V7/IPS1 lower, IPS1/IPS2 upper, IPS2/IPS3 lower.

For probabilistic fibre-tracking we traced 2000 fibres per seed voxel with a maximum of 200 jumps (step size: 0.5 mm, angle threshold: 70°). Free parameters were adjusted so that the convergence of the tracts was heightened and the occurrence of spurious connections was minimized. Probability maps were superimposed on b_0-images with MRIcro (www.mricro.com).

Figure 5. Results of the random saccade experiment for subject S6 rendered on an inflated representation of the cortical surface of the left hemisphere. Regions showing higher activation for saccades than for fixation ($p < 0.001$) are displayed in shades from red to yellow. Map thresholds were chosen so that the activation pattern would match those of the phase-encoded task. The left side shows the medial surface of the hemisphere. Early dorsal and ventral visual areas and the SEF were activated by the random saccade task. On the right the left hemisphere is displayed from a posterio-lateral point of view. A large swath of activation covers the entire IPS and its medial wall and extends up to the postcentral gyrus. A small patch of activation is located near the inferior end of the postcentral gyrus. The FEF is activated at the junction of SFS and PCS along with a second patch of activation located more lateral at the precentral gyrus. (CF = calcarine fissure; CS = central sulcus; FEF = frontal eye fields; IPS = intraparietal sulcus; PCS = precentral sulcus; POS = parieto-occipital sulcus; SEF = supplementary eye fields; SFS = superior frontal sulcus; TOS = trans-occipital sulcus)

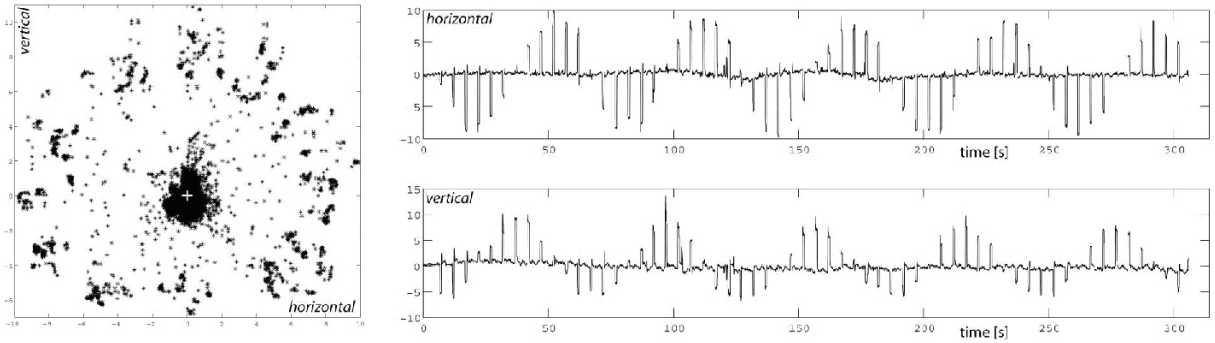

Figure 6. Behavioural data. (A) The scatter plot on the left shows eye positions for a period of 300 s (sample rate, 50 Hz) during the phase-encoded task for subject S5. Saccades were made to all 12 possible locations on the target circle. Saccade amplitudes are slightly deformed in the vertical direction due to shifts in calibration. (B) The right column shows the same data as horizontal and vertical eye position versus time. (horizontal and vertical axis are arbitrary units; artefacts were removed before plotting).

4. Results

4.1 Random saccade paradigm

The random saccade paradigm served to identify the cortical components of the oculomotor system. As expected, saccade-related activations were found throughout the frontoparietal network as well as in the occipital lobe. Figure 5 exemplifies the results with subject S6. All six subjects showed significant activation ($p < 0.001$) in early and mid-level visual areas (V1, V2, V3, V3a, V7) during the random saccade task. Some subjects also showed activation in lateral occipital areas (LO), in superior (ST) and medial temporal areas (MT). Further, all subjects showed activation along the IPS and its medial wall, often extending beyond the anterior end of the sulcus just before the postcentral gyrus. In some subjects this patch of activation extended laterally and included the inferior parts of the postcentral gyrus.

In the frontal lobe, we found significant activation in all subjects near the junction of the superior temporal sulcus (STS) and the precentral sulcus (PCS), where the putative human FEF is located (Corbetta et al., 1998). Often activation extended further lateral along the PCS. All subjects showed activation of the medial wall of the superior frontal gyrus where the putative human SEF is situated (Grosbras et al., 1999). All saccade-related activity was in general bilaterally symmetric, although SEF activation was relatively more pronounced in the left hemisphere in most subjects.

4.2 Phase-encoded paradigm

Continuously varying the angle of the remembered target location allowed us to compute linear correlation maps similar to methodologies used to analyse retinotopy in early visual areas. Eyetracker data confirmed that subjects were able to execute saccades at the right time to the proper locations (Fig. 6). Subject S2 showed unusually noisy linear correlation maps and was therefore excluded from further phase-encoded analysis.

We found several regions in each hemisphere that contained topographic maps of contra-lateral remembered saccade targets. Figure 7 displays the phase-encoded data of all 5 subjects. Upper visual field representations are coloured in red and lower visual field representations are depicted in green. A whole sequence of topographic areas covers the IPS and adjacent regions. Each single topographic area represents the whole contralateral visual hemifield and has an opposite visual field orientation than its neighbours (white arrows). Topographic maps in the frontal cortex were often less clearly defined. Three subjects had a retinotopic FEF in both hemispheres. Subjects S3 and S6 showed phase-encoded activity only in the right hemisphere. Subject S5 showed a second topographic map in the left lateral precentral gyrus (dotted white line). No evidence was found for topography in the SEF.

In the IPS the transition from one area to the next was defined by a reversal in visual field orientation (Schluppeck et al., 2005). To identify the areas we used knowledge about their anatomical location and the visual field orientation. The most clearly discernable area along or near the IPS was area V3A. Located posterior of the caudal tip of the IPS it was largest in extent and clearly visible. Areas anterior of V3A were smaller and often affected by signal dropouts (i.e. the signal was below the statistical threshold). Borders between successive topographic areas were usually

Mean Talairach coordinates of topographic regions

	coordinates (left)				coordinates (right)			
Brain Region	*N*	*x*	*y*	*z*	*N*	*x*	*y*	*z*
V3A	5	-22.4 ± 5.2	-87.2 ± 4.0	10.0 ± 4.5	5	21.0 ± 3.6	-82.0 ± 3.7	15.2 ± 5.5
V7	5	-25.4 ± 0.9	-76.8 ± 5.9	23.0 ± 8.0	5	24.4 ± 4.7	-71.6 ± 6.6	26.2 ±4.9
IPS1	5	-19.0 ± 4.6	-72.4 ± 3.0	35.2 ± 10.7	5	18.8 ± 5.8	-69.8 ± 1.9	37.4 ± 4.7
IPS2	5	-18.6 ± 3.4	-65.8 ± 4.5	44.0 ± 11.6	5	17.2 ± 4.4	-67.0 ± 3.8	48.0 ± 5.7
IPS3	2	-19.0 ± 1.4	-68.0 ± 12.7	44.0 ± 12.7	2	19.0 ± 4.2	-65.5 ± 9.2	49.5 ± 6.4
FEF	3	-24.7 ± 7.0	-9.8 ± 4.4	49.2 ± 2.9	5	24.7 ± 4.2	-11.5 ± 4.1	48.8 ± 5.4

Table 1. Average positions of topographic regions (mm ± SD). The number of hemispheres showing a particular topographic map is indicated (N). x (lateral/medial), y (anterior/posterior), and z (superior/inferior) according to Talairach and Tournoux (1988).

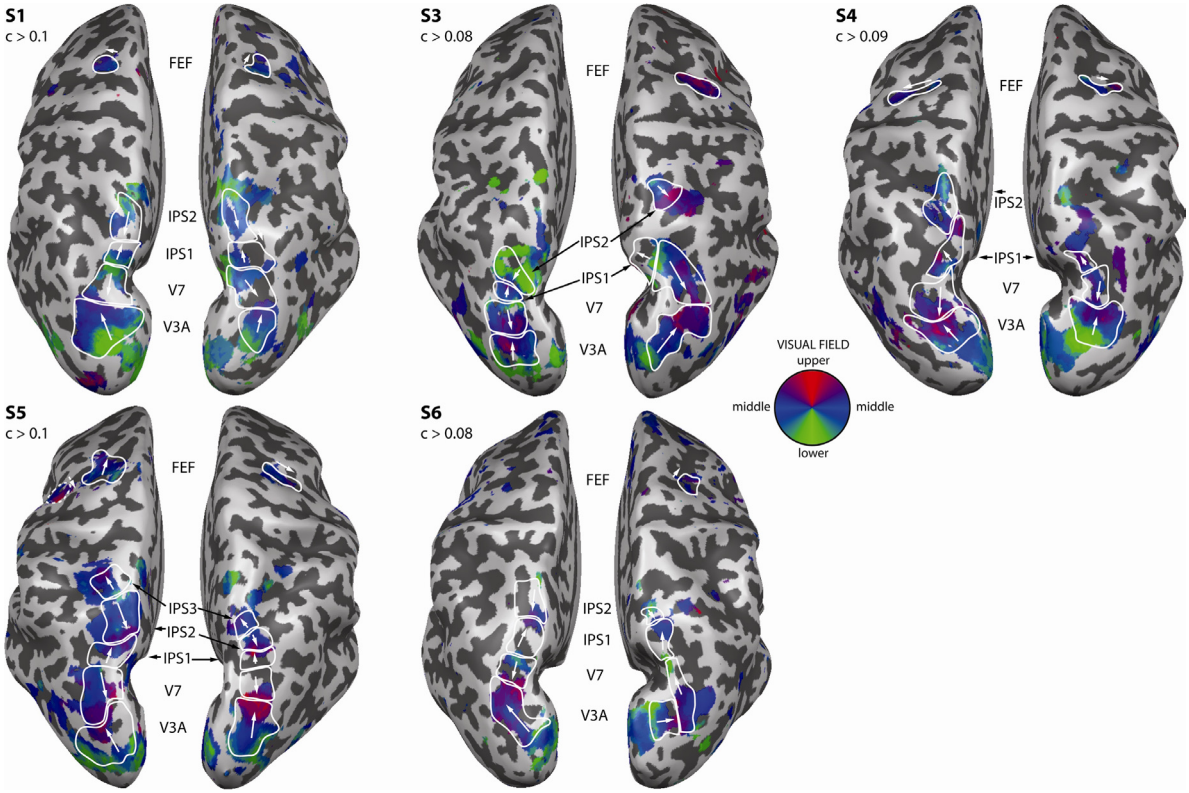

Figure 7. Topography for delayed saccades. Linear correlation maps of the contralateral visual field have been rendered on inflated cortical surface representations. Shown are the dorsal surfaces of each hemisphere for five subjects from a posterior point of view. The hue indicates the response phase. Correlation thresholds were chosen separately for each subject and are indicated. Topographic areas are encircled by a white continues line. The dashed white line indicates a second frontal topographic area found only in subject S5. White arrows point into the direction of the steepest phase gradient of each individual area. They point from lower to upper vertical meridian. Black arrows help to identify the areas.

orthogonal to the orientation of the IPS (i.e. the direction of fastest phase change was tangential to the orientation of the IPS). The whole sequence of bordering topographic maps usually covered more of the medial bank of the IPS than the lateral bank. Relative to anatomical landmarks, there was little variance between the individual subjects regarding the location of periodically activated regions.

We defined the posterior border of area V7 as the anterior border of V3A. The border between V7 and IPS1 was consequently at the next phase gradient reversal, and so on. The posterior parts of areas V7 and IPS2 represent the upper visual field and their anterior parts the lower visual field. The posterior parts of areas V3A, IPS1 and tentative IPS3 represent the lower visual field and their anterior parts the upper visual field (Fig. 7). The

posterior border of V7 was situated at or posterior to the junction of transoccipital sulcus (TOS) and the IPS. In some subjects the sequence of areas V3A, V7, and IPS1 covered the whole extent of the IPS, so that IPS2 was rostral to the anterior tip of the IPS, bordering the postcentral gyrus (S3, S4, S5). Despite the individual differences we report the Talairach coordinates of areas V7, IPS1, and IPS2 for comparison (Table 1). Locations of these areas were symmetric across hemispheres and similar to Schluppeck et al.' findings. Schluppeck et al. found the following coordinates, averaged over eight hemispheres: V7, <±25,-80,27>; IPS1, <± 21, -76, 42>; IPS2, <±18, -71, 52>. The tentative region IPS3 was found in only one subject (S5). It was visible in both hemispheres, had a visual field orientation opposite to IPS2, and its size and significance was comparable to other visuomotor regions in the same subject. The single topographic map found by Sereno et al. was located at <24, -65,53>. Its location was closer to IPS3 (8.4) found in this study than to IPS2 (9.8) (Euclidian distances).

4.3 Fibre-tracking results

Streamline-tracking starting in the FEF often revealed a large tract running from the cortex lateral to the ventricles and then curving medially to the

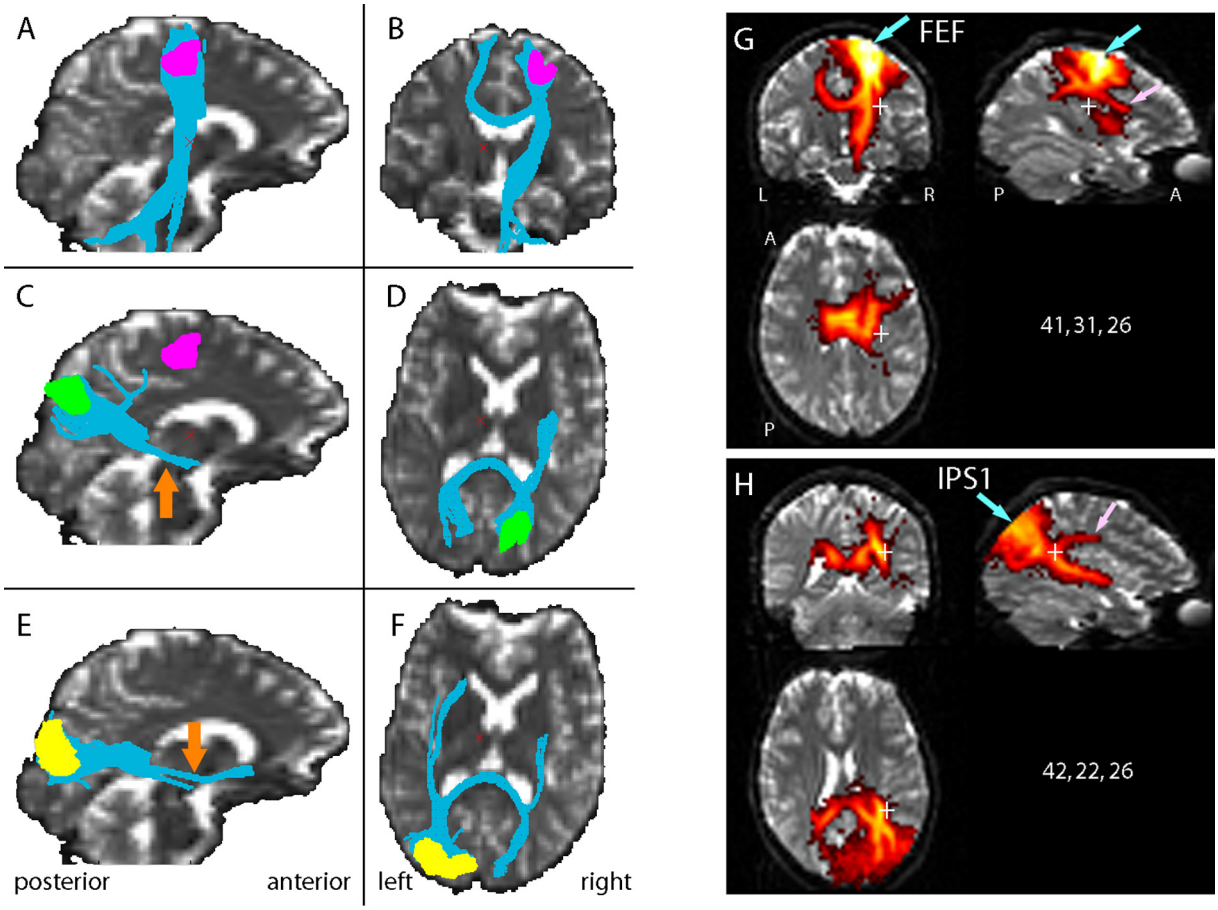

Figure 8. Representative fibre-tracking results for deterministic streamline tracking (left columns) and probabilistic tracking (right column). (A-F) Projection of streamline fibres seeded in respective ROIs of subject S1 onto central b0-slices. (A, B) show fibres originating in the right FEF (pink). (C, D) show fibres originating in the right IPS1 (green). (E, F) show fibres originating in the left V3A (yellow). The left column shows saggital views and the right column axial views except for (B) which shows a coronal view. For reference we indicated FEF also in (C). Orange arrows point to the inferior longitudinal fasciculus. (G, H) Probabilistic tracking results for subject S5. The probability of a connection between the respective seed region and any other voxel in the respective slice is indicated by the hue. Cyan arrows point to the seed region and pink arrows to the superior longitudinal fasciculus (SLF). In (G) the right FEF was seeded. On the coronal slice one can clearly see cross-callosal connections and a tract running from the cortical surface towards the brainstem. The major body of the SLF is revealed by the probabilistic tracking as depicted on the saggital slice. In (H) the right IPS1 was seeded. Posterior parts of the superior and inferior longitudinal fasciculi are tracked. Slice numbers are indicated by a small cross (voxels = 643; voxelsize = 3 mm3; x (saggital slices), y (coronal slices), and z (axial slices)).

brainstem (Fig. 8, A, B). In addition, fibres crossing to the contralateral side were revealed. These fibres most often connected regions located medially of the FEF (B). These fibres did not start in the ROI but were picked up the FEF-ROI, which was in general deeply embedded into a sulcal fundus, when they had already travelled some millimetres through white matter. The probabilistic tracking confirmed these results and in addition revealed a large part of the superior longitudinal fasciculus (SLF) (pink arrow, Fig. 8, G).

Higher visual and visuomotor regions V7, IPS1, IPS2, and IPS3 were connected by the inferior longitudinal fasciculus (ILF) to fronto-temporal regions (orange arrow, Fig. 8, C, D). The posterior part of the fibre bundle between the cortical surface and the posterior end of the ILF was inclined depending on how superior respectively anterior the seed region was situated. Cross-callosal connections, again, terminated in medial regions of the contralateral hemisphere (D). Streamline tracking did not reveal larger parts of the SLF or any other possible connection between IPS and FEF. Figure C, shows one of few rare cases where streamline tracking revealed the most posterior part of the SLF. It does, however, not quite reach the FEF. On the other hand, probabilistic tracking consistently revealed the most posterior part of the SLF (pink arrow, Fig. 8, H). We found no branches that left the central part of the SLF and reached the cortical surface for frontal regions such as the FEF.

Area V3A was connected to fronto-temporal regions by a large fibre bundle, the ILF, running lateral to the posterior horns of the lateral ventricles and lateral to the Putamen (Fig. 8, E, F). The tract often terminated in a hook-like structure in the frontal lobe. Cross-callosal connections were found between regions located medially of left and right V3A.

Connections between adjacent regions (%)

Regions			*left hemisphere*	*right hemisphere*
V3A	→	V7	11.7	7.5
V7	→	V3A	6.2	5.3
V7	→	IPS1	5.4	11.5
IPS1	→	V7	6.6	5.9
IPS1	→	IPS2	13.5	2.0
IPS2	→	IPS1	3.9	1.0
IPS2	→	IPS3	1.1	5.8
IPS3	→	IPS2	2.1	4.9

Table 2. Connections between adjacent areas along the IPS as found by deterministic streamline tracking. The percentage indicated is the ratio between the sum of all fibres that connect two region A with region B and the sum of all fibres leaving the first region A, across all subjects.

The group statistics based on streamline tracking show consistent connections between neighbouring areas in the same hemisphere (Table 2). Excluding IPS3, on average there were 1967 fibres (SD = 899) tracked from each ROI. The great majority of these fibres connected neighbouring regions within the same hemisphere. Three subjects (S2, S5, S6) showed a small number of fibres (1-5) that connected non-neighbouring areas. However, these connections existed only in one direction (A → B) and were not found in the opposite direction (B → A).

The great variability between hemispheres, for example, there are more than six time more connections between IPS1 and IPS2 in the left hemisphere than in the right, can be attributed to the different number of fibres that were seeded in the respective areas (left IPS1, 907; right IPS1, 2058). This might be due to accumulating errors in the chain of image registrations. Functional images were first registered to anatomical images which were then registered to the DTI images. Imprecisely located ROIs might not have penetrated white matter deep enough to initiate fibre propagation. A further source of variance is the highly variable fibre tracking process itself.

Because these results basically contradicted our hypothesis that the anatomical connections between fronto-posterior oculomotor regions can be revealed by DTI, we investigated the tensor maps at specific places in detail. Figure 9 shows an enlarged section of the tensor map of subject S4 on the left and directionally colour-coded FA maps on the right. We hypothesised that the preference of deterministic streamline tracking based on a single-tensor model for following the most dominant fibre direction was the reason for the lacking IPS-FEF connections. This limitation can potentially be overcome by either allowing the tracking algorithm to follow directions distinct from the orientation of the major eigenvector, or by adjusting the model to represent more than one fibre orientation per voxel. The former was done by means of probabilistic tracking, the latter by modelling two tensors per voxel. A combination of both was not available for this study.

As described above, probabilistic tracking revealed parts of the SLF but did not find connections between the IPS and the FEF. On the other hand, two-tensor streamline tracking, as implemented in the Camino software package, turned out to be highly susceptible to noise and generated many spurious connections even after

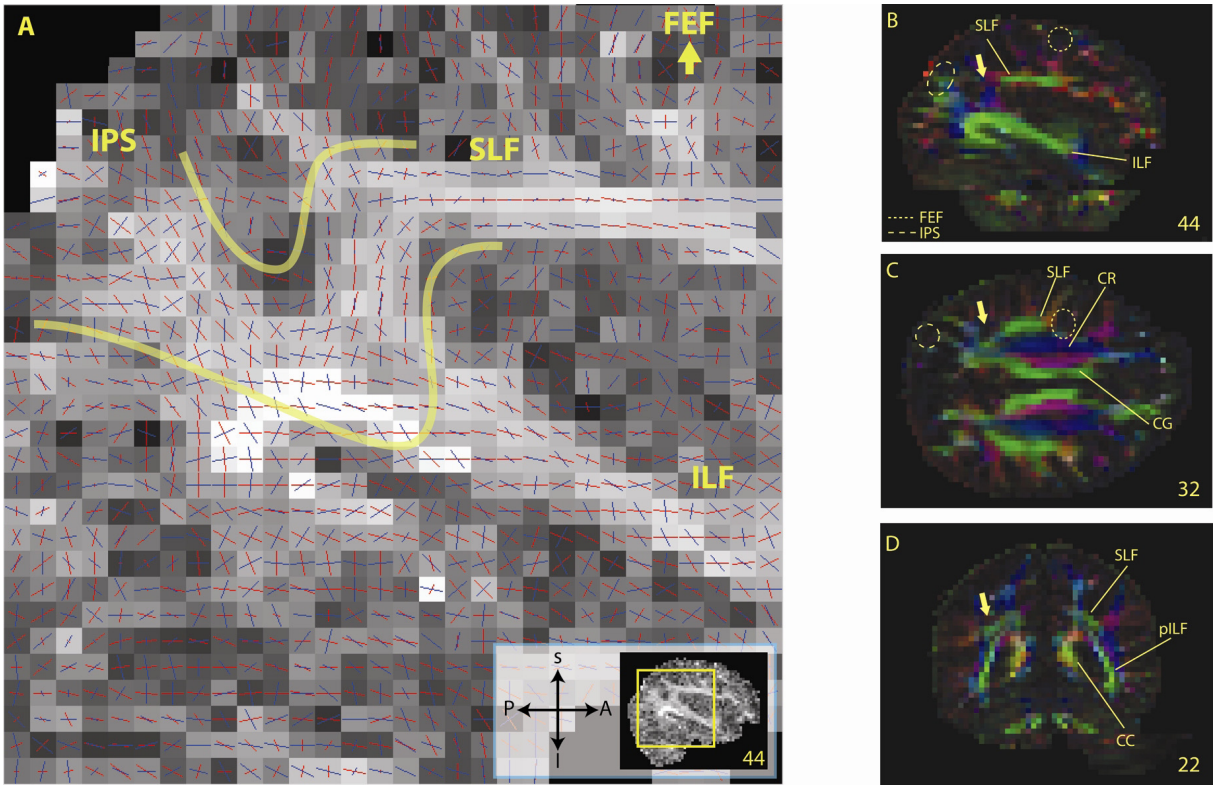

Figure 9. (A) Two-Tensor orientation map overlaid on a fractional anisotropy map of subject S4 (lateral saggital slice). Red and blue lines represent projections of the major eigenvectors of the first and second tensor on the image plain. Brighter shades represent larger FA values and darker shades smaller FA values. The inset shows position of the enlarged section. A possible connection between parietal and frontal areas might be located between the two yellow lines. (B-D) FA maps of single-tensor model, coloured according to the anatomic direction of the major eigenvector of the diffusion tensor (red: left–right, green: anterior–posterior, blue: inferior–superior). (B) shows the same saggital slice as the enlarged section on the right. The ILF and to a lesser extent the SLF contain high FA values and tensors oriented in anterior-posterior direction (bright green). (C) shows a horizontal slice at the height of the SLF. Three different fibre bundles can be identified. Going from medial to lateral one first encounters the fibres of the limbic system running along the medial surface of the hemisphere in anterior-posterior direction (CG, green). The violet and blue coloured regions contain callosal fibres curving upward from the body of the corpus callosum towards the medial surface and ascending cortico-spinal fibres (superior corona radiate, CR). More lateral and posterior the SLF is shown in green. (D) shows a coronal slice at the position indicated by the arrows on the other slices. Posterior-laterally oriented fibres of the corpus callosum (CC) are shown as two yellow compact dots. Lateral are the fibres of the posterior region of ILF. The posterior end of the SLF is located more superior (grey/green).

adjusting the FA and angle thresholds. A detailed analysis of the tensor orientations of a two-tensor model (Fig. 9, A) revealed that a potential connection between IPS and SLF would have to follow the direction of the primary tensors (red) from the IPS until the posterior end of the ILF, then follow the secondary tensors (blue) for three or four voxels, and finally switch back to the primary tensor. In essence, this procedure amounts to a single-tensor model, by setting the orientation of the single tensor to either the orientation of the primary tensor or the orientation of the secondary tensor. Classification of voxels as Gaussian or non-Gaussian, reveals voxels which potentially contain several fibres of different orientations. To avoid tracking in the most dominant direction we set the orientation of the single tensor in all non-Gaussian voxels to the orientation of the secondary tensor of the two-tensor model. In summary, this approach was about tracking into non-dominant directions in all voxels that were assumed to contain more than one fibre orientation, and following the dominant fibre direction in all voxels that were assumed to contain only one fibre orientation. This procedure, however, did not improve on the conventional streamline tracking. We attributed this to the secondary tensor's high susceptibility to noise and the incoherent results of the voxel classification.

Voxel classification depended on arbitrary thresholds and yielded non-Gaussian voxels, which were almost randomly distributed throughout the white matter. Noise-related problems can be potentially overcome by imaging more directions and thereby improving the signal-to-noise ratio and the angular resolution of the two-tensor model.

To sum up, although the quality of the functional results allowed us to define proper seed regions for the fibre-tracking, multiple approaches to reveal fronto-parietal connections between cortical oculomotor regions failed. In the discussion we will try to give reasons for the failure of the methods.

5. Discussion

In this study we combined functional MRI data with DTI-based tractographic data to investigate the anatomical connectivity between cortical oculomotor areas in the healthy human. We successfully located the most important cortical oculomotor areas, such as FEF, SEF, and several areas in the IPS. On the basis of previous findings, we predicted that the FEF and several intraparietal visuomotor areas were retinotopically organized (Hagler and Sereno, 2005; Sereno et al., 2001; Schluppeck et al., 2005). We were able to show significant retinotopy using considerably less saccades (480) than Schluppeck et al. (720-1440). Based on functional results in the human and extrapolating from macaque tracer studies we expected that these areas would be anatomically connected in humans. We hypothesised that a combined DTI-fMRI approach would reveal these connections, especially a fronto-parietal pathway connecting the human homologue of monkey LIP with the FEF. Overall, our tractographic results were negative. Below we will discuss the functional results followed by an in-depth look at the tracking results and an attempt to explain the fact that the hypothesised connections were not found.

5.1 Retinotopic maps

The functional results were in general agreement with previous findings (Schluppeck et al., 2005) with the exception of the unusual layout of retinotopic areas found in subject S5 (Fig. 7). Not only did the subject show a third topographic region anterior of IPS2, but also a second frontal region lateral of the left FEF. Further retinotopic prefrontal regions are usually not activated by a simple delayed-saccade task. Hagler and Sereno (2006) found multiple topographically organized frontal and prefrontal areas using a phase-encoded two-back identity task with faces. The co-activation of regions involved in working memory and processing of more complex stimuli might indicate that the subject used a different processing technique. After all, saccade target locations in a delayed-saccade task could be memorized in a number of ways: visually, as a covert motor program, as a more abstract description of the target position, such as the number on the clock face in the same position (possibly even including verbalization), or as any combination of the above. The design of the present study can, however, not discern between different processing strategies and different functional anatomy.

Position and visual field orientation of the tentative IPS3 region that we found in subject S5 approximately match those of the single topographic region found by Sereno et al. (2001). The visual field orientation of IPS3 is opposite to IPS2 and its location is well anterior to the superior terminus of the parieto-occipital sulcus and slightly closer to the central sulcus than to the occipital pole. It is, however, not clear why a retinotopic area in this region consistently showed up only in Sereno et al.'s study, because the task they used is basically identical to the task used in Schluppeck et al. and the present study. Further, it is puzzling that the latter two studies were able to show IPS1 and IPS2, which were not reported by Sereno et al. Incidentally, although its position has not been reported, IPS3 also seems to show up during Hagler and Sereno's phase-encoded two-back identity task At this point we can only speculate whether the reasons for this discrepancy are of methodological nature, such as different field strengths and acquisition times, or due to other uncontrolled experimental parameters, such as individual differences between subjects and the way they processed the stimuli.

In conclusion, although the functional data confirmed previous findings, inter-subject variability is large. Further experiments are needed to differentiate the multifaceted characteristics of the IPS.

5.2 Limitations of the combined DTI-fMRI approach

Despite its principal limitations, DTI-based

fibre-tracking has successfully identified a larger number of white matter tracts in the healthy human brain (see, e.g., Wakana et al., 2003). Why did the tracking of an IPS-FEF connection through the SLF fail? In general, tracking can fail for a large number of reasons. Some of them are of rather fundamental nature, like the ones described in the introduction, some depend on the specific nature of the tracts that one attempts to reveal, and others depend on the particular combination of MR methods that were used in the present study. In the following we will work out what these limitations are and how they influenced our results.

One should note that there is an important difference between this study and studies that try to reveal major fibre bundles. There is no doubt that DTI-based fibre-tracking has proved to accurately and consistently reveal the fibres of the corpus callosum and the cortico-spinal tract, which have made for numerous cover pictures and illustrations. However, there are essential differences between the present approach and most other tractographic studies. The goal of this study was not to reveal entire anatomical tracts, but to find connections between distinct cortical regions. Studies that aim to create a fibre tract-based atlas (Wakana et al., 2003) track from all pixels inside the brain ("brute force" approach) and then use multiple manually defined ROIs to select the tracts of interest. These so-called multi-ROI approaches use very large, box-shaped seed regions. These ROIs are used in conjunction with logical operators AND, OR, and NOT to select the desired tracts and remove fibres belonging to anatomically different pathways (Mori and Zijl, 2002). To eliminate the subjectivity inherent in this multi-ROI approach we decided against an operator-defined tractography and only use the functionally defined seed regions.

Studies that are interested in tracing connections between specific regions most often define the seed areas in subcortical white matter (Behrens et al., 2003a; Croxson et al., 2005; Johansen-Berg et al., 2005). In general, tracing connections between cortical areas is more difficult and less robust, because the relative low white matter penetration of cortical areas and the high complexity or spreading, as fibres reach grey matter, can mean that the diffusion anisotropy is too low to initiate reliable probabilistic tractography from the cortex (Croxson et al., 2005). Most studies circumvent this problem by either defining subcortical seed regions or using seed regions in white matter fascicles associated with particular cortical regions. We anticipated this difficulty and let the seed regions penetrate into white matter for at least one voxel. Of 49 seed regions only two (4%) did not initiate any fibre tracking. This shows that connections between seed regions could in principle have been found, because seed and target regions contained white matter voxels with FA values high enough to trace fibres.

Figure 9 is an attempt to identify the exact location of the problem and ways to solve it. Fibres seeded in the IPS descend along a vertically oriented tract of reasonably high FA (green/blue, B) until they meet the posterior part of the ILF. Here they should travel in a horizontal direction for the length of two or three voxels before starting to ascend again as illustrated by the enlarged section on the left (A). Indeed, there is a vertical tract where the arrow points at (B). However, instead of ascending, almost all fibres continue following the ILF to the frontal and lateral lobes. This behaviour can be explained by looking at the tensor orientations in detail. A tracking algorithm based on the single tensor model will prefer tracing the ILF over the SLF for two reasons. First, diffusion anisotropy is much higher in the ILF than in its surrounding. Second, the stream-line algorithm used in this study prefers the most collinear tensor orientation. That means that changes in direction with an angle larger than 90° are impossible. A sharper turning angle might be required at the current resolution. In fact, many of the primary tensors that descend from the IPS and from the SLF align almost parallel or in a V-like angle at the posterior tip of the ILF. Because of the collinearity criterion increasing the threshold angle does not help in deterministic streamline tracking.

The situation is quite similar for the FEF, only that here the superior part of the corona radiata (SCR) acts as a sink (blue, Fig. 9, C). Most of the fibres seeded in the FEF initially drift medially and then follow through the internal capsule towards the brain stem. The SCR is by far the most dominant fibre bundle in the dorsal part of the frontal lobe, having coherently oriented tensors and high FA (blue-violet, Fig. 9, C). The FEF is located rostral of the anterior end of the SLF. Although the SLF is known to have projections into the temporal lobe (Mori et al., 2002) these are hardly visible on the FA map and are not picked up by conventional streamline tracking.

The problem can be summarized by an affinity of the deterministic streamline tracking for following the most dominant fibre direction. We hypothesised that it would be possible to improve

the tracking by switching either to a two-tensor model or to probabilistic tracking.

The two-tensor approach, however, failed to locally model two fibre directions. Two-tensor models are usually difficult to estimate, because the fitting process of the tensors is prone to local minima. As a rule, higher *b*-values and a larger number of directions are needed for higher-order models (Frank, 2001). The present study's *b*-value of 1000 s mm^{-2} and 60 directions were sufficient for a single-tensor model, but probably inadequate for higher-order models.

The disappointing performance of the probabilistic tracking can also be attributed to an inadequate local model. If the angular resolution is not sufficient to dissociate several fibre orientations, as depicted in Figure 2 (IIc), or if the model allows only a single tensor, the fitting might yield an indiscriminate disc or sphere-shaped tensor. Although the tensor includes the orientations of secondary fibres *inter alia*, these directions will only be traced on the expense of tracing all other directions represented by the tensor. Thus, probabilistic tracking will trace the correct fibre directions but also give a large number of false-positives. In practice, this yields very diffuse probability maps, in which the seed voxel is connected to a large number of brain areas. Probabilistic fibre-tracking algorithms usually have a number of free parameters which allow adjusting the probability by which less likely fibre directions will be traced, thereby controlling the "sharpness" of the tracts between deterministic and random. However, if the local model is too indiscriminate, adjusting this threshold will be a very delicate procedure and often reveal only the major tracts or diffuse and uninterpretable connections. In addition, it is hard to scientifically justify a certain arbitrary threshold. Unless the model accurately represents the local fibre structure, probabilistic tracking of crossing or branching fibre structures will not lead to robust and reproducible results.

Another explanation for the negative findings is the possible absence of the hypothesised tracts in humans. However this explanation seems unlikely given the abundant evidence in the qualitatively very similar macaque brain (Schall et al., 1995; Stanton et al., 1995; Vincent et al. (unpublished)). In addition, Behrens et al. (2006) could reveal medial portion of the SLF with a probabilistic tractography approach that supports multiple fibres per voxel (Behrens et al. 2003b). They explicitly show that the SLF is invisible to the single fibre approach, because it is obscured by the medial motor projections.

In summary, in the case of single-tensor streamlining, the high FA values and the coherent organization of the tensors contained in the ILF have acted as a sink for the line-propagation. Streamlines that entered the ILF were "caught" in the tract and could not branch off in other directions. This is a deficiency of the deterministic single-tensor streamline tracking, which in general does not allow the tracking of any other than the most dominant fibre direction. In other words, non-dominant fibre directions are obscured by the dominant fibre direction. Probabilistic tracking approaches are based on the very idea of tracking in non-dominant directions. These approaches are doomed to fail if the local model is indiscriminate. The successful tracking of the SLF in Behrens et al. (2006) suggests that a higher resolution ($2 \times 2 \times 2$ mm^3) and averaging over three sets of diffusion-weighted data provides a sufficient basis for subsequent probabilistic tracking of multiple fibres per voxel.

6. Conclusion

Limitations of a combined DTI-fMRI approach can be mainly attributed to limitations of DTI rather than fMRI. DTI suffers, over and above several fundamental methodological limitations (e.g. poor resolution of DTI compared to the size of fibre tracts), from the additional requirements imposed by the cortical seed regions. Fibre tracking in its current state is much more suited to study the properties of white matter tracts isolated from their cortical targets rather than the connections between specific cortical regions. That is why most of the applied DTI-based fibre-tracking studies have focused on tracking significant white matter fascicles to either classify them (Wakana et al., 2003) or to analyse their properties during development and in presence of lesions (Guye et al., 2003; Munakata et al., 2006; Schonberg et al. 2006).

The fundamental lesson to be learnt from this study is that DTI-based fibre-tracking is in need of further methodological development to overcome the limitations inherent in the method and to be up to the additional requirements of specific cortico-cortical tracking. Major improvements are needed regarding the three limitations presented in the introduction: data, model, and tracking. The resolution and SNR of the diffusion weighted images has to improve to be able to dissociate

complex fibre structures near the cortical surface and in regions of crossing fibres. The diffusion model has to represent the underlying fibre structure as close as possible and optimally improve the tracking by removing redundant information. The tracking should support tracing fibres through regions of crossing and branching fibres, yield a connection probability map, and represent fibres in a way that matches their natural appearance.

Substantial improvements are already expected by switching from a single-tensor model to a model that represents multiple fibre orientation per voxel and by switching from deterministic to probabilistic tracking. Of course, the quality of the data (i.e. number of directions, *b*-value, SNR) has to support this. Single-tensor deterministic tracking is certainly not adequate for the tracking of long-range cortico-cortical connections through regions of crossing or branching fibres.

Nevertheless, once these problems have been overcome, a combination of fMRI and DTI-based tractography seems to be a most promising area of application. The mapping of both, functional active areas and their anatomical connections, in vivo, will help us to better understand functional and anatomical connectivity and thus enable much more comprehensive models of the brain.

Acknowledgements

I would like to thank both my supervisors – Pieter Medendorp and David Norris – for their outstanding support during the course of this challenging project. Furthermore, I would like to acknowledge Hubert Fonteijn's help with the technical aspects of the analysis and Paul Gaalman's help with the scanning. I am more than thankful for the support and suggestions of the F. C. Donders' MR group. Last but not least I would like to thank Ian Fitzpatrick for his comments on the first draft of this thesis.

References

Alexander, D. C., Barker, G. J., & Arridge, S. R. (2002). Detection and modeling of non-Gaussian apparent diffusion coefficient profiles in human brain data. Magn Reson Med, 48(2), 331-340.

Alexander, D. C. (2006). An introduction to computational diffusion MRI: the diffusion tensor and beyond. In "Visualization and image processing of tensor fields" edited by J.Weickert and H.Hagen, Springer 2006.

Astafiev, S. V., Shulman, G. L., Stanley, C. M., Snyder, A. Z., Van Essen, D. C., & Corbetta, M. (2003). Functional organization of human intraparietal and frontal cortex for attending, looking, and pointing. J Neurosci, 23(11), 4689-4699.

Baker, J. T., Patel, G. H., Corbetta, M., & Snyder, L. H. (2006). Distribution of activity across the monkey cerebral cortical surface, thalamus and midbrain during rapid, visually guided saccades. Cereb Cortex, 16(4), 447-459.

Bammer, R., Acar, B., & Moseley, M. E. (2003). In vivo MR tractography using diffusion imaging. Eur J Radiol, 45(3), 223-234.

Basser, P. J., Pajevic, S., Pierpaoli, C., Duda, J., & Aldroubi, A. (2000). In vivo fiber tractography using DT-MRI data. Magn Reson Med, 44(4), 625-632.

Beaulieu, C. (2002). The basis of anisotropic water diffusion in the nervous system - a technical review. NMR Biomed, 15(7-8), 435-455.

Behrens, T. E., Johansen-Berg, H., Woolrich, M. W., Smith, S. M., Wheeler-Kingshott, C. A., Boulby, P. A., et al. (2003a). Non-invasive mapping of connections between human thalamus and cortex using diffusion imaging. Nat Neurosci, 6(7), 750-757.

Behrens et al., 2003b T.E.J. Behrens, M.W. Woolrich, M. Jenkinson, H. Johansen-Berg, R.G. Nunes, S. Clare, P.M. Matthews, J.M. Brady and S.M. Smith, Characterization and propagation of uncertainty in diffusion-weighted MR imaging, Magn. Reson. Med. 50 (2003), pp. 1077–1088

Behrens, T. E., Johansen-Berg, H., Jbabdi, S., Rushworth, M. F. S., Woolrich, M. W. (2006). Probabilistic diffusion tractography with multiple fibre orientations: What can we gain? NeuroImage, 34(1), 144-155.

Boynton, G. M., Engel, S. A., Glover, G. H., & Heeger, D. J. (1996). Linear systems analysis of functional magnetic resonance imaging in human V1. J Neurosci, 16(13), 4207-4221.

Burgel, U., Amunts, K., Hoemke, L., Mohlberg, H., Gilsbach, J. M., & Zilles, K. (2006). White matter fiber tracts of the human brain: three-dimensional mapping at microscopic resolution, topography and intersubject variability. Neuroimage, 29(4), 1092-1105.

Cook, P. A., Bai, Y., Nedjati-Gilani, S., Seunarine, P. A., Hall, M. G., Parker, G. J., Alexander, D. C. (2006). Camino: Open-Source Diffusion-MRI Reconstruction and Processing, 14th Scientific Meeting of the International Society for Magnetic Resonance in Medicine, Seattle, WA, USA, 2759.

Croxson, P. L., Johansen-Berg, H., Behrens, T. E., Robson, M. D., Pinsk, M. A., Gross, C. G., et al. (2005). Quantitative investigation of connections of the prefrontal cortex in the human and macaque using probabilistic diffusion tractography. J Neurosci, 25(39), 8854-8866.

Dougherty, R. F., Ben-Shachar, M., Bammer, R.,

Brewer, A. A., & Wandell, B. A. (2005). Functional organization of human occipital-callosal fiber tracts. Proc Natl Acad Sci U S A, 102(20), 7350-7355.

Frank, L. R. (2001). Anisotropy in high angular resolution diffusion-weighted MRI. Magn Reson Med, 45(6), 935-939.

Guye, M., Parker, G. J., Symms, M., Boulby, P., Wheeler-Kingshott, C. A., Salek-Haddadi, A., et al. (2003). Combined functional MRI and tractography to demonstrate the connectivity of the human primary motor cortex in vivo. Neuroimage, 19(4), 1349-1360.

Hagler, D. J., Jr., & Sereno, M. I. (2006). Spatial maps in frontal and prefrontal cortex. Neuroimage, 29(2), 567-577.

Jezzard, P., & Balaban, R. S. (1995). Correction for geometric distortion in echo planar images from B0 field variations. Magn Reson Med, 34(1), 65-73.

Johansen-Berg, H., Behrens, T. E., Robson, M. D., Drobnjak, I., Rushworth, M. F., Brady, J. M., et al. (2004). Changes in connectivity profiles define functionally distinct regions in human medial frontal cortex. Proc Natl Acad Sci U S A, 101(36), 13335-13340.

Jones, D. K., Horsfield, M. A., & Simmons, A. (1999). Optimal strategies for measuring diffusion in anisotropic systems by magnetic resonance imaging. Magn Reson Med, 42(3), 515-525.

Koch, M. A., Norris, D. G., & Hund-Georgiadis, M. (2002). An investigation of functional and anatomical connectivity using magnetic resonance imaging. Neuroimage, 16(1), 241-250.

Koyama, M., Hasegawa, I., Osada, T., Adachi, Y., Nakahara, K., & Miyashita, Y. (2004). Functional magnetic resonance imaging of macaque monkeys performing visually guided saccade tasks: comparison of cortical eye fields with humans. Neuron, 41(5), 795-807.

Le Bihan, D. (2003). Looking into the functional architecture of the brain with diffusion MRI. Nat Rev Neurosci, 4(6), 469-480.

Lewis, J. W., & Van Essen, D. C. (2000a). Mapping of architectonic subdivisions in the macaque monkey, with emphasis on parieto-occipital cortex. J Comp Neurol, 428(1), 79-111.

Lewis, J. W., & Van Essen, D. C. (2000b). Corticocortical connections of visual, sensorimotor, and multimodal processing areas in the parietal lobe of the macaque monkey. J Comp Neurol, 428(1), 112-137.

Mori, S., Kaufmann, W. E., Davatzikos, C., Stieltjes, B., Amodei, L., Fredericksen, K., et al. (2002). Imaging cortical association tracts in the human brain using diffusion-tensor-based axonal tracking. Magn Reson Med, 47(2), 215-223.

Mori, S., & van Zijl, P. C. (2002). Fiber tracking: principles and strategies - a technical review. NMR Biomed, 15(7-8), 468-480.

Munakata, M., Onuma, A., Takeo, K., Oishi, T., Haginoya, K., & Iinuma, K. (2006). Morphofunctional organization in three patients with unilateral polymicrogyria: combined use of diffusion tensor imaging and functional magnetic resonance imaging. Brain Dev, 28(6), 405-409.

Munoz, D. P. (2002). Commentary: saccadic eye movements: overview of neural circuitry. Prog Brain Res, 140, 89-96.

Ogawa, S., Lee, T. M., Kay, A. R., & Tank, D. W. (1990). Brain magnetic resonance imaging with contrast dependent on blood oxygenation. Proc Natl Acad Sci U S A, 87(24), 9868-9872.

Orban, G. A., Van Essen, D., & Vanduffel, W. (2004). Comparative mapping of higher visual areas in monkeys and humans. Trends Cogn Sci, 8(7), 315-324.

Parmar, H., Sitoh, Y. Y., & Yeo, T. T. (2004). Combined magnetic resonance tractography and functional magnetic resonance imaging in evaluation of brain tumors involving the motor system. J Comput Assist Tomogr, 28(4), 551-556.

Reese, T. G., Heid, O., Weisskoff, R. M., & Wedeen, V. J. (2003). Reduction of eddy-current-induced distortion in diffusion MRI using a twice-refocused spin echo. Magn Reson Med, 49(1), 177-182.

Schall, J. D. (2004). On the role of frontal eye field in guiding attention and saccades. Vision Res, 44(12), 1453-1467.

Schall, J. D., Morel, A., King, D. J., & Bullier, J. (1995). Topography of visual cortex connections with frontal eye field in macaque: convergence and segregation of processing streams. J Neurosci, 15(6), 4464-4487.

Schluppeck, D., Glimcher, P., & Heeger, D. J. (2005). Topographic organization for delayed saccades in human posterior parietal cortex. J Neurophysiol, 94(2), 1372-1384.

Schonberg, T., Pianka, P., Hendler, T., Pasternak, O., & Assaf, Y. (2006). Characterization of displaced white matter by brain tumors using combined DTI and fMRI. Neuroimage, 30(4), 1100-1111.

Sereno, M. I., Pitzalis, S., & Martinez, A. (2001). Mapping of contralateral space in retinotopic coordinates by a parietal cortical area in humans. Science, 294(5545), 1350-1354.

Sereno, M. I., & Tootell, R. B. (2005). From monkeys to humans: what do we now know about brain homologies? Curr Opin Neurobiol, 15(2), 135-144.

Silver, M. A., Ress, D., & Heeger, D. J. (2005). Topographic maps of visual spatial attention in human parietal cortex. J Neurophysiol, 94(2), 1358-1371.

Smith, S. M. (2002). Fast robust automated brain extraction. Hum Brain Mapp, 17(3), 143-155.

Stanton, G. B., Bruce, C. J., & Goldberg, M. E. (1995). Topography of projections to posterior cortical areas from the macaque frontal eye fields. J Comp Neurol, 353(2), 291-305.

Talairach, J., & Tournoux, P. (1988). Co-planar stereotaxic atlas of the human brain : 3-dimensional proportional system : an approach to medical cerebral imaging. Stuttgart

Tuch, D. S. (2004). Q-ball imaging. Magn Reson Med, 52(6), 1358-1372.

Vincent, J. L., Patel, P. H., Fox, M. D., Snyder, Baker, Snyder, Corbetta, Raichle (submitted) The Intrinsic Functional Architecture of the Primate Oculomotor Network.

Wakana, S., Jiang, H., Nagae-Poetscher, L. M., van Zijl, P. C., & Mori, S. (2004). Fiber tract-based atlas of human white matter anatomy. Radiology, 230(1), 77-87.

Weickert, J., & Hagen, H. (2006). Visualization and processing of tensor fields. Berlin: Springer.